Porous TiO_2 with a controllable bimodal pore size distribution from natural ilmenite

Tao Tao,[ab] Alexey M. Glushenkov,*[a] Qiyuan Chen,[b] Huiping Hu,[b] Dan Zhou,[cd] Hongzhou Zhang,[cd] Markus Boese,[d] Sanly Liu,[e] Rose Amal[e] and Ying Chen[a]

Received 13th August 2010, Accepted 11th October 2010
DOI: 10.1039/c0ce00533a

Ilmenite ($FeTiO_3$) is an inexpensive abundant natural mineral and it would be a perfect precursor for the production of porous TiO_2 if a suitable synthesis method was developed. A new method combining a series of processing steps of ball milling, high-temperature annealing, selective chemical leaching and final calcining in air is proposed in this paper. The resulting TiO_2 is a porous material with a bimodal pore structure. The pore size distribution has two clear maxima corresponding to small mesopores (2–30 nm) and large meso- and macropores (centered at around 50–80 nm). It was found that the duration of the annealing step could alter the contribution of each type of pores. A short annealing time (0.5 h) lead to the preferential formation of pores within 2–30 nm while pores centered at 50–80 nm dominated the pore size distribution after a relatively long annealing (1.5 h). The obtained porous rutile TiO_2 shows a better photocatalytic activity than that of a commercial rutile TiO_2 powder.

1. Introduction

Porous titania (TiO_2) has applications in solar cells, photocatalysts, and lithium-ion batteries.[1–4] The porous structure plays an important role in these applications because it provides a larger surface area and often a well-defined characteristic pore size. For example, it has been reported that the photoelectric conversion efficiency of a dye-sensitised solar cell prepared using mesoporous TiO_2 nanoparticles as an electrode material was 10.1%, exceeding the efficiency of the reference cell based on P25 (nonporous TiO_2 nanopowder) by 3.8%.[2] Hierarchically micro-/nano-porous TiO_2 films have an improved photocatalytic activity in mineralizing gaseous acetaldehyde and liquid-phase phenol with respect to that of non-porous films, because the continuous pore channels in the porous TiO_2 film enhance the transportation of reactants, products and O_2 within the catalytic framework.[3]

A number of synthetic methods have been proposed for obtaining porous titanium dioxide. They often involve the use of templates and include (but are not limited to) hydro- and solvothermal methods, sol–gel synthesis, evaporation-induced self-assembly and application of ionic liquids.[5–12] In many cases the titanium precursors or templates used for preparing porous TiO_2 (for example, tetraisopropyl-orthotitanate,[13] titanium tetraisopropoxide,[14] cetyltrimethylammonium bromide (CTAB),[15] mesoporous silicas SBA-15 or KIT-6[16]) are not readily available or expensive materials.

Ilmenite ($FeTiO_3$), naturally occurring iron titanate, is cheap, abundant, and suitable for producing titanium dioxide. The US Geological Survey[17] states that the world total reserves of ilmenite are above 680 million tons (containing about 350–400 million tons of TiO_2) and the deposits of ilmenite can be found in different parts of world – North America (USA, Canada), South America (Brazil), Australia, Asia (China, India, and Vietnam), Europe (Norway, Ukraine) and Africa (South Africa, Mozambique). According to the same source, the price of ilmenite is low and was fluctuating between 80 and 107 USD per ton between 2004 and 2008. At present, ilmenite is commonly used in industry for making white pigment *via* a sulfate or chlorine route.[18,19] It would be very desirable to adapt the existing industrially applicable techniques to the preparation of porous TiO_2 suitable for advanced applications.

In the current paper we demonstrate a method capable of preparing TiO_2 with porous structure from ilmenite. The method includes *carbothermal reduction*, *ball milling* and *acid leaching*.

Carbothermal reduction is a process in which ilmenite is reduced by carbon to yield metallic iron and titanium oxide at high temperatures. *Ball milling* is capable of reducing the temperature needed for carbothermal reduction of ilmenite and increasing the rate of this reaction.[20] Chen *et al.* have reported that a ball milled mixture of $FeTiO_3$ and activated carbon can react and produce rutile TiO_2 at a temperature as low as 760 °C.[21] The effects of the pre-treatment of ilmenite by ball milling on its refinement can be attributed to the creation of crystal defects and lattice distortions, the decrease in particle sizes and the increase of surface areas.[21,22] A parametric study of the mechanically activated carbothermal reduction of ilmenite has been published by Welham.[23]

Recently, single-crystalline TiO_2 nanorods have also been produced using the ball milling and annealing process.[24] The low temperature treatment in hydrogen atmosphere activates

[a]*Institute for Technology Research and Innovation, Deakin University, Waurn Ponds, VIC 3217, Australia. E-mail: alexey.glushenkov@deakin.edu.au; Fax: +61 3 52271103; Tel: +61 3 52272931*
[b]*College of Chemistry and Chemical Engineering, Central South University, Changsha, 410083, China*
[c]*School of Physics, Trinity College Dublin, Dublin 2, Republic of Ireland*
[d]*Centre for Research on Adaptive Nanostructures and Nanodevices (CRANN), Trinity College Dublin, Dublin 2, Republic of Ireland*
[e]*School of Chemical Engineering, ARC Centre of Excellence for Functional Nanomaterials, The University of New South Wales, Sydney, NSW 2052, Australia*

controlled one-dimensional growth of TiO_2 crystals. Hydrogen gas prevents the formation of three-dimensional structures at the nanometer scale.

Acid leaching has been widely used in industries in order to remove iron and impurities and obtain high grade titanium dioxide. The leaching with hydrochloric acid is more attractive because it removes impurities (such as Ca^{2+}, Mg^{2+}, *etc*) more efficiently and the acid can be easily recovered from waste solutions.[25–27] Acid leaching can also involve direct dissolution of the metallic iron if ilmenite is fully or partially reduced to metallic iron and titanium oxide by a preliminary step such as carbothermal reduction.

In the following sections, we describe a method for the preparation of porous TiO_2 from ilmenite. A combination of ball-milling, carbothermal reduction, acid leaching and eventual calcining in air is used. The method leads to the formation of porous TiO_2 with a bimodal distribution of pores, where smaller pores are holes in single-crystalline nanoparticles and the larger pores are spaces between nanoparticles in larger aggregates. The formation of porous structure is discussed. The porous structure of produced TiO_2 leads to a higher photocatalytic activity than that of a commercial rutile TiO_2.

2. Experimental

2.1 Synthesis of porous TiO_2

The preparation of porous TiO_2 included the following steps:

(1) Ball milling of a mixture of ilmenite and an activated carbon
(2) Annealing
(3) Leaching by acid
(4) Calcining in air

Ball Milling. 6 grams of a mixture of ilmenite ($FeTiO_3$, 99% purity, supplied by Consolidated Rutile Ltd, Australia) and activated carbon (10–18 mesh granular activated charcoal, supplied by BDH Chemicals Ltd., England) were milled in a stainless steel container loaded with four hardened steel balls (diameter of 25.4 mm).[28] The weight ratio of $FeTiO_3$ to carbon was 4 : 1. The composition of the ilmenite used in this work can be expressed as TiO_2 (dry basis) 49.6%, iron (total) 35.1%, FeO 32.8%, Fe_2O_3 13.7%, Al_2O_3 0.47%, Cr_2O_3 0.25%, SiO_2 0.45%. The milling was conducted for 150 h at room temperature under argon atmosphere of 100 kPa. The milling time can be reduced if a high-speed milling instrument is used.

Annealing. 2 g of the milled mixture were heated in a horizontal tube furnace from room temperature to 1000 °C within 30 min and held at 1000 °C for 60 min. The sample was allowed to cool down to room temperature afterwards. The whole experiment was conducted under a flow of Ar gas.

Leaching. 1 g of annealed sample was leached in 100 ml of 4M HCl solution at 90 °C for 4 h. The process was performed in a paraffin oil bath and under magnetic stirring of 800 rpm. After leaching, the suspension was filtered, and the leached samples were washed and dried at 90 °C for 4 h.

Calcining. The leached sample was subsequently calcined in air at 600 °C for 2 h in order to remove the residual activated carbon from the sample.

2.2 Characterization

The samples were characterized by X-ray diffraction (XRD, Philips 3020 diffractometer, Co target, $\lambda = 0.1789$ nm), scanning electron microscopy (SEM, Carl Zeiss Supra55vp and UltraPlus instruments) and transmission electron microscopy (TEM, FEI Titan microscope operating under 300 kV). Energy-dispersive X-ray spectrometry (EDS) was conducted within a scanning electron microscope in order to obtain elemental composition. Surface areas, pore volumes and pore size distributions of the samples were determined using a Micromeritics Tristar 3000 adsorption instrument. The diffuse reflectance spectra of dry powders were measured using a Cary 300 UV-Vis spectrophotometer (Varian) equipped with an integrating sphere. $BaSO_4$ was used as a reference sample.

2.3 Photocatalytic measurements

The photocatalytic activity of the samples was measured using a small batch photocatalytic reaction system which consisted of a photoreactor with a near-UV illumination source and a conductivity monitor for measuring carbon dioxide generated as the organic substance was oxidised. A 20 W NEC black-light blue fluorescent lamp was used as the light source. This lamp has a wavelength emission peak at approximately 370 nm and emits radiation between 320 nm and 410 nm. The catalyst loading was 1 g l^{-1} and the volume of the reaction mixture was 100 ml. Phenol was chosen as the model organic compound. The amount of phenol mineralised was equivalent to 1000 μg of carbon. The photocatalytic reaction was initiated by turning on the UV lamp. The detailed description of the process has been given by Matthews.[29] A commercial pure rutile TiO_2 powder (particle size < 100 nm, surface area > 130 m^2 g^{-1}) from Sigma Aldrich was also tested for comparison.

3. Results and discussion

Fig. 1a shows a SEM image of starting ilmenite, which consists of large particles with a typical size of 100 μm and varied shapes. Ball milling of the mixture of ilmenite and activated carbon and subsequent annealing of the ball milled mixture lead to significant changes in both morphology and phase composition.

The product of annealing of milled mixtures of $FeTiO_3$ and C at 1000 °C for 1 h, which is shown by the SEM image in Fig. 1b, consists of much smaller particles (with sizes between 10 nm and 1 μm). The XRD pattern of the milled sample (Fig. 2a) shows predominantly the peaks of the $FeTiO_3$ phase, and the amorphous phase of the activated carbon does not contribute to the pattern. The broadening of peaks of $FeTiO_3$ is caused by the crystal size reduction induced by the ball milling treatment.[30] The XRD pattern of the annealed sample (Fig. 2b) shows peaks of rutile TiO_2, α-Fe and another phase, which was identified as γ-Fe(C) (austenite). The pattern also shows the presence of a certain amount of unreduced ilmenite ($FeTiO_3$) in the sample.

Fig. 3 shows a SEM image of the material obtained after acid leaching of the annealed sample and subsequent calcining in air. The obtained product consists of particles with a submicron average size, as shown in Fig. 3. As we demonstrate below by TEM, many of these particles are in fact aggregates of smaller single-crystalline nanoparticles with a porous structure.

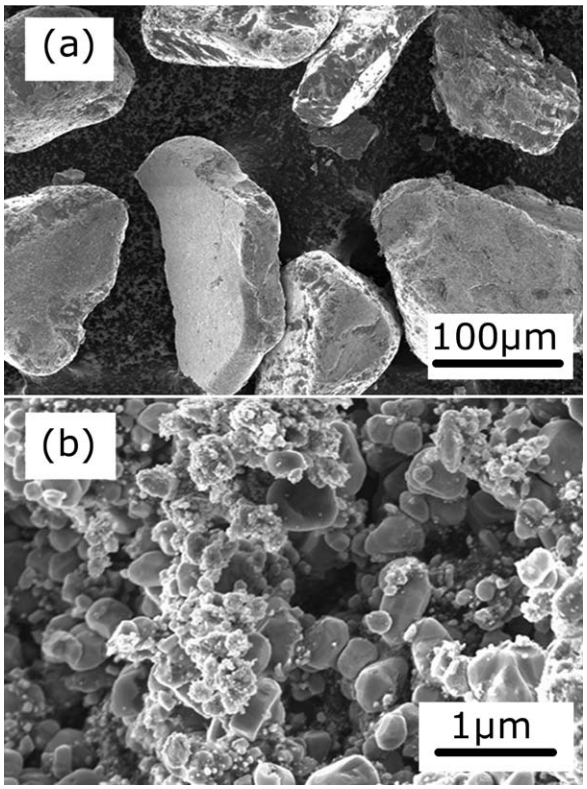

Fig. 1 SEM images of starting ilmenite (a) and the powder product obtained after ball milling and annealing of the mixture of ilmenite and activated carbon (b).

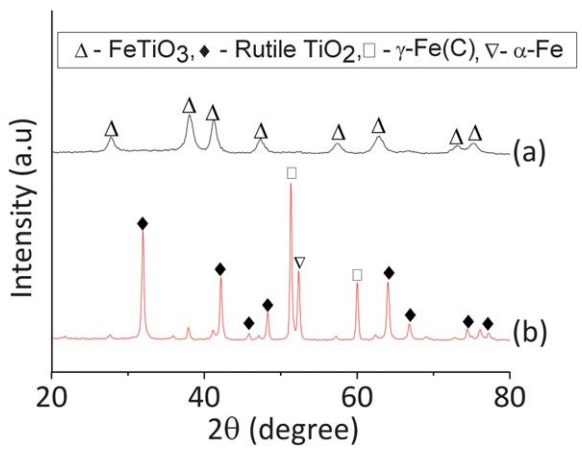

Fig. 2 XRD patterns of the milled mixture of ilmenite and carbon (a) and the product of subsequent annealing of this mixture at 1000 °C in Ar gas for 1 h (b).

Indeed, the TEM images of this material are shown in Fig. 4. A large cluster in the bright field image (Fig. 4a) consists of nano-sized particles with a typical size of less than 100 nm. Fig. 4b is the selected area electron diffraction pattern (SADP) taken from the cluster and it confirms that the particles belong to the rutile phase. The polycrystalline nature of the SADP demonstrates that the nanoparticles aggregate randomly to form the large cluster. A typical particle is shown in Fig. 4c. The bright areas (such as the one indicated by the white arrows) are thin electron transparent

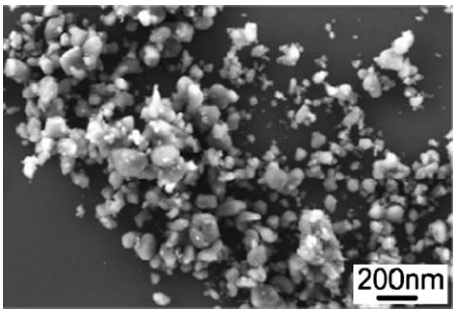

Fig. 3 SEM image of the material obtained from the annealed sample (1000 °C, Ar atmosphere, 1 h) after leaching and calcining.

regions in the particle. The image reveals the high density of pores on the particle and that the size of them can be down to several nanometers. A high-resolution TEM image of the particle and its nanopores is shown in Fig.4d. Nanodiffraction was also performed on the particle, and the existence of the rutile phase was verified. The part enclosed by the white frame is magnified in the inset of Fig. 4d. The lattice spacings of the horizontal and slanted fringes are 0.23 and 0.28 nm, respectively, and correspond to the {200} and {101} planes. It is worth pointing out that the lattice fringes are running through the pore area (single-crystallinity) and the variation of contrast may be due to the difference in thickness introduced by the pores.

The pore size distribution of the obtained porous TiO_2 is shown in Fig. 5a. The distribution is bimodal with the first peak at between 2 and 20 nm (small mesopores) and the second peak at between 25 and 150 nm (the range of large meso- (<50 nm) and macro- (>50 nm) pores). It is easy to understand by correlating the pore size distribution with the results of TEM (Fig. 4) that the

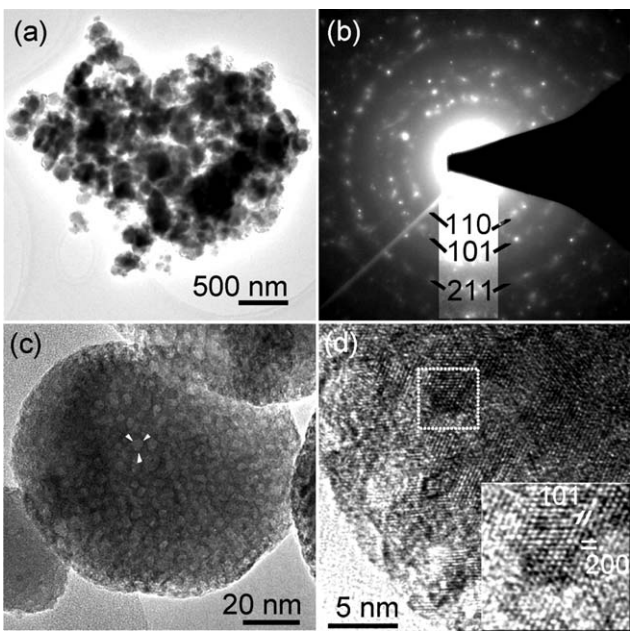

Fig. 4 TEM characterization of porous TiO_2 obtained after annealing (1000 °C, Ar atmosphere, 1 h), leaching and calcining of the ball milled mixture. (a) A bright-field image of an aggregate of nanoparticles, (b) the SADP of the aggregate indicating randomly oriented rutile TiO_2 crystallites, (c) nanosized pores in an individual nanoparticle, and (d) the lattice image of the nanoparticle.

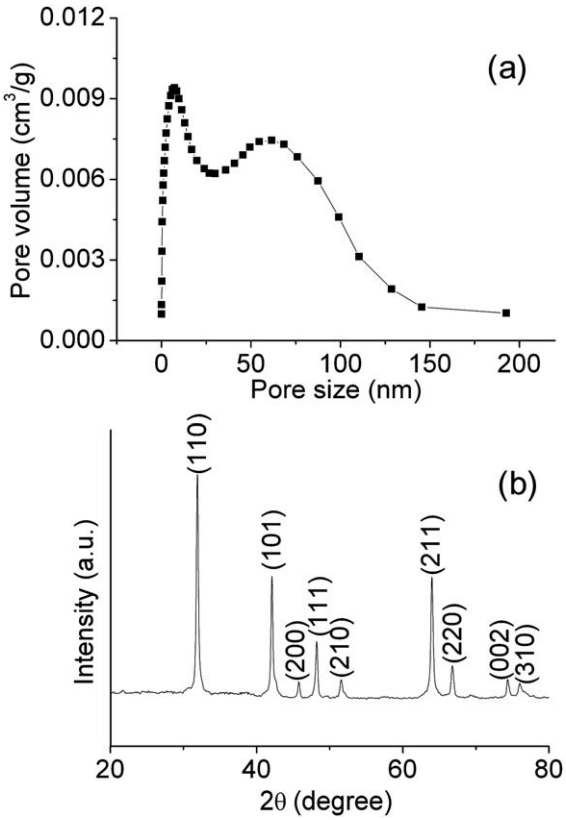

Fig. 5 Pore size distribution (a) and XRD pattern (b) of porous rutile TiO_2 obtained after annealing (1000 °C, Ar atmosphere, 1 h), leaching and calcining of the ball milled mixture.

small mesopores in the distribution correspond to the pores within individual nanoparticles while the second range of larger pores represents spaces between nanoparticles in aggregates. The XRD pattern (Fig. 5b) shows the presence of the rutile TiO_2 phase (JCPDS file no. 01-077-0440) only, which is consistent with the data of electron diffraction. Based on the above results, we conclude that the procedure consisting of ball milling of carbon/ilmenite mixtures, annealing, acid leaching and calcining is a viable way to produce porous rutile TiO_2 with a bimodal pore structure.

Table 1 shows the surface areas and total pore volumes of three samples at various stages of this synthesis, particularly, after ball milling, leaching and final calcining. It is apparent that the acid leaching leads to a significant increase in the surface area and total pore volume. More specifically, the surface area increases to 46.9 $m^2\ g^{-1}$, and the pore volume reaches 0.155 $cm^3\ g^{-1}$. The final step of calcining in air at 600 °C leads to the decrease in the surface area to the value of 22.8 $m^2\ g^{-1}$. This is caused by a combined effect of the removal of residual carbon component

Table 1 Surface area and pore volume of samples at different stages of synthesis

Samples	Surface area ($m^2\ g^{-1}$)	Total pore volume ($cm^3\ g^{-1}$)
milled	13.2	0.044
leached	46.9	0.155
calcined	22.8	0.141

from the sample and the sintering of TiO_2 particles during heat treatment. Li *et al.*[31] have also reported that certain degree of sintering and possible increase in the particle size happen in the course of annealing of TiO_2 obtained from acid leaching of ball milled ilmenite at 600 °C.

It is clear to us that the annealing step (carbothermal reduction) controls the formation of small mesopores in our porous TiO_2. In order to discriminate the role of the carbothermal reduction, the annealing time was varied while all other parameters and steps of the synthesis were kept unchanged. The phase composition of the samples after annealing in Ar was monitored by XRD, and the resulting pore size distributions were analyzed.

The XRD patterns of samples after annealing at 1000 °C for different lengths of time (0.5, 1 and 1.5 h) in Ar flow are presented in Fig. 6. 0.5 h is not long enough for the significant reduction of ilmenite by carbon at 1000 °C. The dominating phase in the XRD pattern (Fig. 6a) is $FeTiO_3$, and only weak peaks of rutile TiO_2 and γ-Fe(C) (austenite) are visible. The reduction of ilmenite is much more pronounced after 1 h of annealing (Fig. 6b). The XRD pattern is dominated by TiO_2, α-Fe and γ-Fe(C) phases, and weak peaks of residual ilmenite are visible. The relative intensity of $FeTiO_3$ peaks with respect to the dominant phases decreases further after 1.5 h of annealing. In addition, the fraction of γ-Fe(C) decreases and that of α-Fe increases.

Fig. 7 displays the pore size distributions of porous TiO_2 samples produced after 0.5 and 1.5 h of annealing and subsequent leaching and calcining. The pore size distribution of the sample obtained after annealing for 1 h, leaching and calcining is also shown again as a dashed line for comparison. All distributions are characterized by the presence of two types of pores (small mesopores at 2–20 nm and large meso- and macro-pores centered at about 40–90 nm) while the relative intensities of two main peaks are varied. When the sample was annealed in Ar for 0.5 h before leaching and calcining, the pores are predominantly in the range of small mesopores (5–40 nm with a maximum at about 10–15 nm), and the second peak centered at 70 nm is not pronounced strongly. When the mixture of ilmenite and carbon was annealed for 1.5 h, the contribution of small mesopores is insignificant and the porosity is dominated by pores of 40–90 nm.

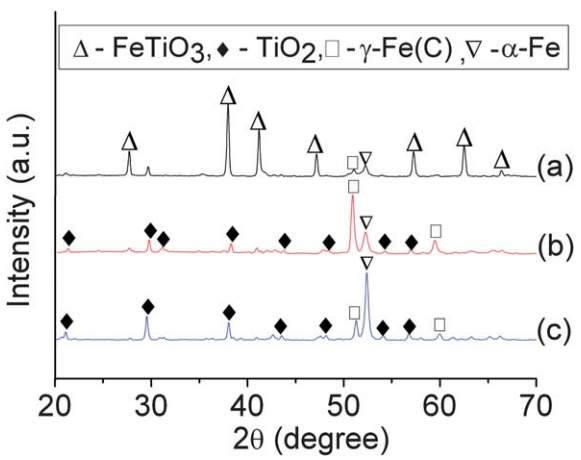

Fig. 6 XRD patterns of the milled mixtures of ilmenite and carbon annealed for different periods of time at 1000 °C: (a) 0.5 h; (b) 1 h; (c) 1.5 h.

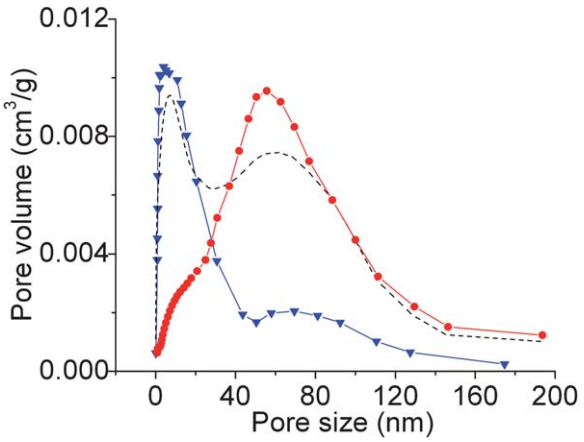

Fig. 7 Pore size distributions of porous samples obtained after annealing for various periods of time, 0.5 h (▼) or 1.5 h (●), and subsequent leaching and calcining. The distribution of the sample annealed for 1 h, then leached and calcined is also shown for comparative purposes (a dashed line). The experimental conditions other than the time of annealing were kept the same.

The pore size distribution of the sample obtained after 1 h of annealing and subsequent leaching/calcining is bimodal with a pronounced contribution from both pore ranges.

By comparing the pore size distribution of porous TiO_2 with the data of TEM we have concluded previously that the range of pores with a maximum at around 50–80 nm corresponds to the spaces between individual nanoparticles in agglomerates, and the pore range of 2–20 nm corresponds to small pores within individual nanoparticles. It is apparent, therefore, that a longer annealing time (1.5 h) leads to the aggregates of almost non-porous nanoparticles, while a short annealing time (0.5 h) leads to relatively large particles with well-developed mesopores of 2–30 nm. When the sample is annealed for 1 h, the pore size distribution is intermediate – bimodal, and the sample is composed from aggregates of porous nanoparticles such as those shown in Fig. 4.

The fractions of small mesopores (2–30 nm) and large meso- and macro-pores (centered at around 50–80 nm) can obviously be adjusted by controlling annealing time. According to the XRD data shown in Fig. 6, the length of carbothermal reduction is correlated with the degree of ilmenite reduction, *i.e.* the amount of ilmenite in the sample after annealing. If $FeTiO_3$ is still a dominant phase in the sample (0.5 h of annealing), small mesopores (2–30 nm) are dominant, while long (1.5 h) annealing time leads to the formation of non-porous nanoparticles. An intermediate time of annealing of 1 h (and, in other words, an intermediate ratio of ilmenite to the products of reduction) leads to the formation of aggregates of porous nanoparticles, a sample with a bimodal distribution of nanoscale pores, where large pores represent the space between nanoparticles and small mesopores correspond to the pores within individual nanoparticles. In accordance with our results, we believe that aggregates of TiO_2 nanoparticles form *via* an attack of acid on iron formed by the reduction of ilmenite into TiO_2 and Fe, while the development of small mesopores within nanoparticles is relevant to the acid leaching of iron directly from ilmenite. To support our argument, we also note that an extended time of acid leaching (4 h) was required in order to develop small pores in our TiO_2 samples.

Formation of porous rutile TiO_2 by leaching of ball milled ilmenite in a diluted H_2SO_4 acid has been observed by Li's group,[31] and can be treated as indirect evidence for the possible contribution of direct leaching of the ball milled $FeTiO_3$ to the formation of small mesopores. Porous TiO_2 with pores of less than 10 nm has been formed in their study, and hydrolysis and precipitation of dissolved titanium have been proposed as a mechanism for the formation of small pores. On the other hand, diluted HCl acid has been found inefficient for the preparation of a highly porous TiO_2, which is not in an agreement with our findings. The interaction of diluted HCl solutions with ilmenite can depend on a number of factors such as structural features of a ball milled $FeTiO_3$, milling mode and atmosphere, presence of carbon, temperature of leaching and acid concentration. We are currently in the process of studying the leaching behaviour of ball milled ilmenite in diluted HCl, and the results are expected to be published shortly.

The photocatalytic properties of porous rutile TiO_2 were compared with those of a commercial rutile powder purchased from Sigma-Aldrich (particle size < 100 nm, surface area > 130 $m^2\ g^{-1}$). One of the key factors controlling a photocatalytic reaction is the light absorption by the catalyst and the migration of the light-induced electrons and holes, which are related to the electronic structure characteristics of the materials. UV-Vis diffuse reflectance spectroscopy was used to characterise the optical absorption properties of the porous and commercial rutile powders, and the spectra are displayed in Fig. 8. The onset wavelengths of the band gap absorption for commercial rutile and porous TiO_2 are approximately 360 nm and 458 nm, respectively. The commercial rutile powder does not exhibit any absorption in the visible light regime ($\lambda > 400$ nm). A red shift in the band gap transition can be seen for the porous TiO_2, implying that there could be defects or impurities (due to iron or carbon incorporated during the synthesis process), resulting in charge transfer between the impurity band and the conduction band of TiO_2. Moreover, the porous rutile TiO_2 shows an enhanced optical absorbance in the wavelength range greater than 320 nm. Although it is outside the scope of the present study, the shift of the porous TiO_2 response to higher wavelengths also implies the possibility of photocatalytic activity under visible light irradiation.

The results of the comparative tests of photocatalytic activity of porous TiO_2 and a commercial rutile TiO_2 are given in Fig. 9. The photocatalytic performance of the particles is compared on

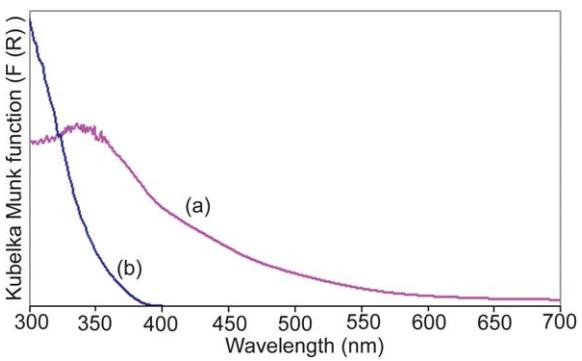

Fig. 8 UV-Vis diffuse reflectance spectra for (a) porous TiO_2; (b) a commercial rutile powder.

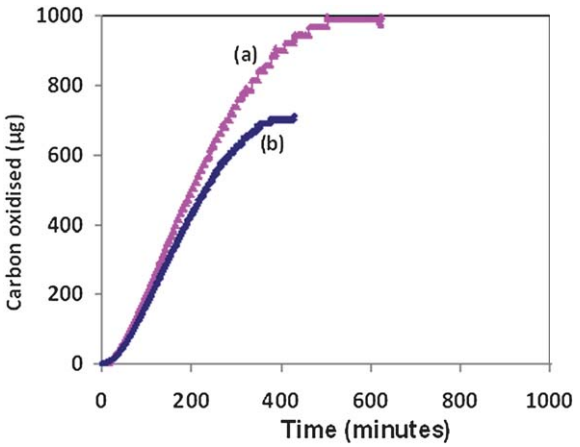

Fig. 9 The results of photocatalytic tests for the mineralisation of phenol with: (a) porous TiO_2; (b) a commercial rutile powder. Total carbon loading in each experiment was 1000 μg.

the basis of the generation rate of carbon dioxide during the oxidation of phenol as a model organic compound. The results reveal that the kinetics of the phenol mineralisation with porous TiO_2 is comparable with that of the commercial rutile TiO_2. However, the porous TiO_2 is able to mineralise all the organic carbon added to the reaction. The photocatalytic activity of TiO_2 depends on various parameters including crystallinity, surface area, structure, additives and density of surface hydroxyl groups.[32] The morphology of the TiO_2 powder is also one of important factors influencing the photocatalytic activity. It has been shown that porous titania photocatalysts possess an increased light absorption resulting in an improved photocatalytic performance.[33] This is consistent with our data, as demonstrated in the stronger absorption in the UVA region for the porous rutile powder (Fig. 8). Since both samples were rutile phase, the variation in photocatalytic activity could not originate from the difference in crystal phase.

4. Conclusions

A method for obtaining porous TiO_2 from natural ilmenite has been proposed in this paper. The method includes four steps: ball milling of a mixture of ilmenite and activated carbon, annealing of the ball milled mixture at 1000 °C in an inert atmosphere, acid leaching and calcining of the final product in air. The electron microscopy study has demonstrated that the product of this method consists of aggregates of porous nanoparticles. The corresponding pore size distribution is bimodal where the typical range of small (3–20 nm) pores corresponds to holes within nanoparticles, and the typical range centered at 50–80 nm is due to the spaces between nanoparticles in aggregates. We believe that the aggregates of TiO_2 nanoparticles form *via* an attack of acid on iron formed by the reduction of $FeTiO_3$ into TiO_2 and Fe, and the development of small mesopores is relevant to the acid leaching of iron directly from ilmenite. The contribution of two types of pores can be adjusted by controlling the time of carbothermal reduction. In addition, it has been demonstrated that the obtained porous TiO_2 is more active than a commercial rutile powder in the photocatalytic degradation of phenol.

Acknowledgements

Financial support from the Australian Research Council is acknowledged. Mr Tao Tao thanks the National Basic Research Program of China (No: 2007CB613601) and the China Scholarship Council (CSC) for providing his scholarship. The work conducted in Trinity College Dublin is supported by the Irish Government's Programme for Research in Third Level Institutions, Cycle 4, National Development Plan 2007–2013 within the framework of the INSPIRE programme and Science Foundation Ireland under Grant 07/SK/I1220a.

Notes and references

1 J. L. Li, L. D. Wang, X. M. Kong, B. B. Ma, Y. T. Shi, C. Zhan and Y. Qiu, *Langmuir*, 2009, **25**, 11162–11167.
2 D. Zhao, T. Y. Peng, L. L. Lu, P. Cai, P. Jiang and Z. Q. Bian, *J. Phys. Chem. C*, 2008, **112**, 8486–8494.
3 Y. Zhao, X. T. Zhang, J. Zhai, J. L. He, L. Jiang, Z. Y. Liu, S. Nishimoto, T. Murakami, A. Fujishima and D. B. Zhu, *Appl. Catal., B*, 2008, **83**, 24–29.
4 W. B. Yue, C. Randorn, P. S. Attidekou, Z. X. Su, J. T. S. Irvine and W. Z. Zhou, *Adv. Funct. Mater.*, 2009, **19**, 2826–2833.
5 R. Tan, Y. He, Y. Zhu, B. Xu and L. Cao, *J. Mater. Sci.*, 2003, **38**, 3973–3978.
6 C. Wang, Z. Deng and Y. Li, *Inorg. Chem.*, 2001, **40**, 5210–5214.
7 G. J. D. A. A. Soler-Illia, A. Louis and C. Sanchez, *Chem. Mater.*, 2002, **14**, 750–759.
8 J. C. Yu, L. Zhang and J. Yu, *New J. Chem.*, 2002, **26**, 416–420.
9 K. S. Yoo, T. G. Lee and J. Kim, *Microporous Mesoporous Mater.*, 2005, **84**, 211–217.
10 C. Su, C. M. Tseng, L. F. Chen, B. H. You, B. C. Hsu and S. S. Chen, *Thin Solid Films*, 2006, **498**, 259–265.
11 J. Jiao, Q. Xu and L. Li, *J. Colloid Interface Sci.*, 2007, **316**, 596–603.
12 H. X. Li, Z. F. Bian, J. Zhu, D. Q. Zhang, G. S. Li, Y. N. Huo, H. Li and Y. F. Lu, *J. Am. Chem. Soc.*, 2007, **129**, 8406–8407.
13 R. Rossmanith, C. K. Weiss, J. Geserick, N. Hüsing, U. Hörmann, U. Kaiser and K. Landfester, *Chem. Mater.*, 2008, **20**, 5768–5780.
14 D. S. Kim, S. J. Han and S. Y. Kwak, *J. Colloid Interface Sci.*, 2007, **316**, 85–91.
15 T. Peng, D. Zhao, K. Dai, W. Shi and K. Hirao, *J. Phys. Chem. B*, 2005, **109**, 4947–4952.
16 W. B. Yue, X. X. Xu, J. T. S. Irvine, P. S. Attidekou, C. Liu, H. Y. He, D. Y. Zhao and W. Z. Zhou, *Chem. Mater.*, 2009, **21**, 2540–2546.
17 U.S. Department of the Interior, *U.S. Geological Survey, Mineral Commodity Summaries*, 2009. (http://minerals.usgs.gov/minerals/pubs/commodity/titanium/mcs-2009-timin.pdf).
18 T. Chernet, *Miner. Eng.*, 1999, **12**, 485–495.
19 T. K. Pong, J. Besida, T. A. O'Donnell and D. G. Wood, *Ind. Eng. Chem. Res.*, 1995, **34**, 308–313.
20 Y. Chen, T. H. Hwang and J. S. Williams, *Mater. Lett.*, 1996, **28**, 55–58.
21 Y. Chen, T. H. Hwang and J. S. Williams, *Metall. Mater. Trans. A*, 1997, **28**, 1115–1121.
22 C. Li, B. Liang and S. P. Chen, *Hydrometallurgy*, 2006, **82**, 93–99.
23 N. J. Welham, *Miner. Eng.*, 1996, **9**, 1189–1200.
24 J. Yu, Y. Chen and A. M. Glushenkov, *Cryst. Growth Des.*, 2009, **9**, 1240–1244.
25 M. R. Lanyon, T. Lwin and R. R. Merritt, *Hydrometallurgy*, 1999, **51**, 299–323.
26 T. A. I. Lasheen, *Hydrometallurgy*, 2005, **76**, 123–129.
27 C. Li, B. Liang and H. Y. Wang, *Hydrometallurgy*, 2008, **91**, 121–129.
28 Y. Chen, T. Halstead and J. S. Williams, *Mater. Sci. Eng., A*, 1996, **206**, 24–29.
29 R. W. Matthews, *J. Catal.*, 1988, **111**, 264–272.
30 Y. Chen, J. S. Williams, S. J. Campbell and G. M. Wang, *Mater. Sci. Eng., A*, 1999, **271**, 485–490.
31 C. Li, B. Liang, H. Song, J. Q. Xu and X. Q. Wang, *Microporous Mesoporous Mater.*, 2008, **115**, 293–300.
32 J. Wang, D. N. Tafen, J. P. Lewis, Z. L. Hong, A. Manivannan, M. J. Zhi, M. Li and N. Q. Wu, *J. Am. Chem. Soc.*, 2009, **131**, 12290–12297.
33 F. Iskandar, A. B. D. Nandiyanto, K. M. Yun, C. J. Jr. Hogan, K. Okuyama and P. Biswas, *Adv. Mater.*, 2007, **19**, 1408–1412.